Mathematical Models and Methods in Applied Sciences
Vol. 29, No. 5 (2019) 939–966

DOI: 10.1142/S0218202519410045

Modeling and simulation of bridge-section buffeting response in turbulent flow

Tore A. Helgedagsrud
Department of Structural Engineering,
Norwegian University of Science and Technology (NTNU),
Richard Birkelands v 1a, Trondheim NO-7491, Norway
tore.a.helgedagsrud@ntnu.no

Yuri Bazilevs*
School of Engineering, Brown University,
184 Hope Street, Providence, RI 02912, USA
yuri_bazilevs@brown.edu

Kjell M. Mathisen
Department of Structural Engineering,
Norwegian University of Science and Technology (NTNU),
Richard Birkelands v 1a, Trondheim NO-7491, Norway
kjell.mathisen@ntnu.no

Jinhui Yan
Department of Civil and Environmental Engineering,
University of Illinois at Urbana-Champaign,
Newmark 2106, 205 N. Mathews, Urbana, IL 61801, USA
yjh@illinois.edu

Ole A. Øseth
Department of Structural Engineering,
Norwegian University of Science and Technology (NTNU),
Richard Birkelands v 1a, Trondheim NO-7491, Norway
ole.oiseth@ntnu.no

Received 12 December 2018
Revised 2 January 2019
Accepted 23 January 2019
Published 3 April 2019
Communicated by K. Takizawa

Buffeting analysis plays an important role in the wind-resistant design of long-span bridges. While computational methods have been widely used in the study of self-excited forces on bridge sections, there is very little work on applying advanced simulation to

---

*Corresponding author

buffeting analysis. In an effort to address this shortcoming, we developed a framework for the buffeting simulation of bridge sections subjected to turbulent flows. We carry out simulations of a rectangular bridge section with aspect ratio 10 and compute its aerodynamic admittance functions. The simulations show good agreement with airfoil theory and experimental observations. It was found that inflow turbulence plays an important role in obtaining accurate wind loads on the bridge sections. The proposed methodology is envisioned to have practical impact in wind engineering of structures in the future.

Keywords: Turbulence; buffeting; bridge aerodynamics; RBVMS; multi-domain modeling; weak boundary conditions; isogeometric analysis.

AMS Subject Classification: 65M60, 76F65, 74F10

1. Introduction

Buffeting analysis plays an important role in the wind-resistant design of long-span bridges and other line-like structures, particularly in serviceability and fatigue limit states.

As for most wind engineering aspects of bridges, buffeting theory originates from the developments in the aerospace engineering and sciences. The earliest formulation was reported in Ref. 1, in which the evolution of the aerodynamic lift on an airfoil was defined for a uniform vertical gust. In Ref. 2 the work was extended to define a function that relates a sinusoidal variation of the vertical wind velocity to a fluctuating lifting force, i.e. the Sears function. A spectral form of the Sears function represents the earliest version of the aerodynamic admittance function, and is still commonly regarded as the reference solution in buffeting analysis.

Unlike airfoils, bridge decks and bluff bodies with detached flows do not have an analytical basis for buffeting, and, therefore, rely on empirical relations. Such a framework was first presented in Ref. 3, where a frequency-domain analysis of buffeting and the concept of aerodynamic admittance were applied to bridges. This methodology was further developed in Refs. 4–7, and, in addition to time-domain methods,[8] presents a standard approach in bridge design today.

Aerodynamic admittances were traditionally obtained from wind tunnel experiments, and several test strategies report successful results, see, e.g. Refs. 9–15. However, as the majority of these methods measure forces over a wider segment than the flow integral length scale, span-wise coherence of the turbulence and buffeting forces must be considered. As discussed in Refs. 15 and 16, this introduces some uncertainty in the estimation of admittance functions. Whereas methods based on pressure strips do not have these problems, they do instead suffer from inaccuracies of the pressure integration.[17]

In contrast to experimental approaches, high-fidelity computational fluid dynamics (CFD) modeling does not suffer from these shortcomings, which makes it a good candidate for buffeting analysis. CFD methods have been widely used in the study of self-excited forces on bridge sections, see e.g. Refs. 18–25 and references therein. For buffeting analysis, however, the only application of CFD, to the best of the authors' knowledge, may be found in Refs. 26 and 27. Although synthetic inlet turbulence was considered in the simulations, the simulations themselves were carried out in 2D, which only gives a limited representation of the dynamics of turbulent flows.

In this work, we present a computational framework, and carry out numerical simulations of buffeting. For the flow simulation, we use the semi-discrete version of the residual-based variational multiscale (RBVMS) formulation of the Navier–Stokes equations of incompressible flows, proposed and further developed in Refs. 28–35. The space–time version of RBVMS, named ST-VMS, was proposed and further developed more recently in Refs. 36–41. Both VMS formulations proved their accuracy and efficiency through numerous high-Reynolds-number flow computations for applications such as parachutes,[42–49] turbomachinery,[50–54] thermo-fluids,[55,56] flows with topology change,[57–64] wind turbines,[65–69] hydro turbines,[70] bio-inspired propulsion,[71–73] cardiovascular hemodynamics[74–77] and bridge aerodynamics.[21,78]

To simulate the incident turbulence, a multi-domain modeling (MDM) approach[79–82,68] is employed, where the turbulence is generated in a separate domain, and then used as the inflow boundary condition (BC) for the bridge-section domain. The incident turbulence is generated by a pressure-driven turbulent channel flow[28,29,83] computed using Isogeometric Analysis (IGA) based on non-uniform rational B-splines (NURBS).[84,85] The flow bulk velocity and friction-velocity-based Reynolds number are used as two parameters that define the turbulent inflow and, in part, govern the turbulence intensity.

To demonstrate the accuracy and efficiency of the framework, aerodynamic admittance functions and pressure distributions on a rectangular section with aspect ratio 1:10 subjected to uniform and turbulent inflow conditions are computed. Although most long-span bridges have a more streamlined shape, rectangular sections are often considered as a reference, and have been extensively studied both experimentally[86,10,87] and numerically.[19,21,88] In addition, as experience has shown,[19,89] accurately capturing the flow separation and reattachment for this geometrically simple bluff-body shape is a challenging task. The bridge section is simulated using standard low-order finite elements (FEM), and the framework of weakly-enforced essential BCs[90–92] is employed to couple the non-matching IGA and FEM discretizations.

The paper is outlined as follows. Section 2 gives an overview of the buffeting theory for bridge sections. In Sec. 3, we present the computational framework. Numerical results are shown in Sec. 4 for the turbulent channel flow and in Sec. 5 for the bridge section. Conclusions are drawn in Sec. 6.

2. Buffeting and Aerodynamic Admittance

Wind loads acting on line-like bridge girders are nonlinear functions of structural motions and incident turbulence. These are, however, commonly linearized

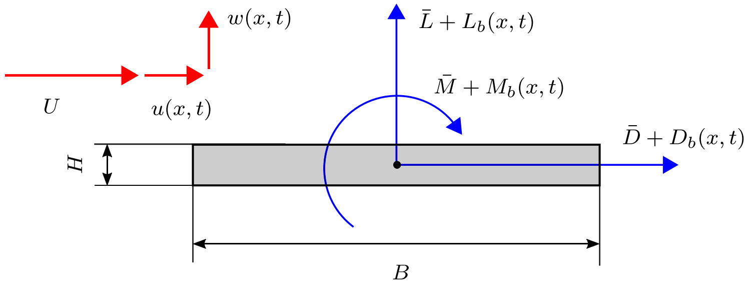

Fig. 1. Aerodynamic forces on a motionless bluff body subjected to a turbulent wind field.

and expressed in terms of time-averaged static, self-excited and buffeting components.[3,93,6] In this work, we focus on the latter. For a comprehensive description of the dynamic wind loads on bridges, the readers is referred to Refs. 4, 94 and 95.

As shown in Fig. 1, we decompose the wind speed into a mean component U, acting in the drag direction of the bridge, and zero-mean turbulent fluctuations $\mathbf{u}(t) = [u, w]^T$ in the drag and lift direction, respectively. Under the assumption of isotropic turbulence, these components are regarded as independent.[96]

The total aerodynamic forces due to a turbulent wind field, $\mathbf{q}_T(t)$, are given as

$$\mathbf{q}_T(t) = \overline{\mathbf{q}} + \mathbf{q}_b(t), \tag{2.1}$$

where $\overline{\mathbf{q}} = [\bar{D}, \bar{L}, \bar{M}]^T$ contains the mean drag, lift and pitching moment, respectively, and $\mathbf{q}_b(t) = [D_b, L_b, M_b]^T$ is the buffeting component.

The drag, lift and pitching-moment coefficients are defined as

$$C_D = \frac{\bar{D}}{1/2\rho U^2 H}, \quad C_L = \frac{\bar{L}}{1/2\rho U^2 B}, \quad C_M = \frac{\bar{M}}{1/2\rho U^2 B^2}, \tag{2.2}$$

where $1/2\rho U^2$ is the stagnation pressure and H and B are the height and the width of the bridge girder, respectively. For the buffeting part we denote $\mathbf{G}_v(K) = [G_u, G_w]^T$ the temporal Fourier transform of $\mathbf{u}(t)$ as a function of the reduced frequency $K = \omega B/U$, and $\mathbf{G}_b(K) = [G_D, G_L, G_M]^T$ the Fourier transform of $\mathbf{q}_b(t)$. The buffeting wind action can then be expressed in the following form[97]:

$$\mathbf{G}_b(K) = \frac{1}{2}\rho U B \boldsymbol{\chi}(K)\mathbf{G}_v(K), \tag{2.3}$$

where

$$\boldsymbol{\chi} = \begin{bmatrix} 2(H/B)\bar{C}_D\chi_{Du} & ((H/B)C'_D - \bar{C}_L)\chi_{Dw} \\ 2\bar{C}_L\chi_{Lu} & (C'_L + (H/B)\bar{C}_D)\chi_{Lw} \\ 2B\bar{C}_M\chi_{Mu} & BC'_M\chi_{Mw} \end{bmatrix} \tag{2.4}$$

is the matrix of aerodynamic admittances. The bars and primes on the aerodynamic load coefficients refer to their mean value and inclination with respect to the angle-of-attack, respectively. The coefficients χ_{ij}, $i \in \{D, L, M\}$, $j \in \{u, w\}$, are the aerodynamic admittance functions, varying with the frequency of the turbulent fluctuations.[98] These can be interpreted as transfer functions between the fluctuating wind velocities and aerodynamic forces.

The cross-spectral density matrix from Eq. (2.3) reads

$$\mathbf{S}_b(K) = \left(\frac{1}{2}\rho U B\right)^2 \boldsymbol{\chi}(K)\mathbf{S}_v(K)\boldsymbol{\chi}^{*T}(K), \tag{2.5}$$

where $\mathbf{S}_b(K)$ and $\mathbf{S}_v(K)$ are the cross-spectral density matrices of the forces and velocities, respectively, and superscript * denotes the complex conjugate of its attribute. Equation (2.5) serves as a starting point for most methods of identifying the aerodynamic admittance functions, such as auto-spectral methods[11,17] and cross-spectral methods.[99]

In the following, we assume that the velocity cross spectrum can be neglected, i.e. $S_{uw}(K) = 0$. Further, we recognize that, for the symmetric bridge section considered in this work, the components $\bar{C}_L$, $\bar{C}_M$ and C'_D are exactly zero. The diagonal components of Eq. (2.5) then reduce to

$$S_{DD}(K) = \left(\frac{1}{2}\rho U B\right)^2 \left(2\frac{H}{B}\bar{C}_D\right)^2 |\chi_{Du}|^2 S_{uu}(K), \tag{2.6a}$$

$$S_{LL}(K) = \left(\frac{1}{2}\rho U B\right)^2 \left(C'_L + \frac{H}{B}\bar{C}_D\right)^2 |\chi_{Lw}|^2 S_{ww}(K), \tag{2.6b}$$

$$S_{MM}(K) = \left(\frac{1}{2}\rho U B\right)^2 (C'_M)^2 |\chi_{Mw}|^2 S_{ww}(K). \tag{2.6c}$$

We note that Eq. (2.6) coincides with the auto-spectral method in buffeting analysis, in which the admittance components χ_{Du}, χ_{Lw} and χ_{Mw} are treated independently. This is also the governing equation for identifying the aerodynamic admittance functions.

For an airfoil passing through a sinusoidal vertical-gust pattern, the analytical expression for the lift admittance is given by the Sears function[2]

$$\chi_{Lw}(K) := \chi(K) = \frac{2}{\pi K H_+(K)}, \tag{2.7}$$

where H_+ is the Bessel function of the third kind. Being derived from a smooth and fully correlated flow, it is a good approximation for streamlined decks and often regarded as the reference solution, however, for bluff bodies it may underestimate the admittance for low frequencies.[10]

Lastly, it should be mentioned that simplified models of buffeting use admittances of unity. This corresponds to quasi-steady theory, and represents the upper bound for the buffeting forces and are often used in design codes (see, e.g. Ref. 100). However, as demonstrated in Ref. 99, this simplification may render an excessive buffeting response.

Remark 2.1. To simplify the above relations we have intentionally omitted the span-wise coordinate. However, in a modal superposition approach, which is a widely used method in structural dynamics, the extension is straightforward. See, e.g. Ref. 4 for a practical implementation.

3. Modeling and Discretization Approaches

3.1. *Navier–Stokes equations of incompressible flows*

We consider the weak formulation of the Navier–Stokes equations for incompressible flows[101] on the domain Ω. Let $\mathcal{S}$ and $\mathcal{V}$ denote the trial and test function spaces, respectively. The variational formulation is then stated as follows: Find a velocity-pressure pair $\{\mathbf{u}, p\} \in \mathcal{S}$, such that for all test functions $\{\mathbf{w}, q\} \in \mathcal{V}$

$$B(\{\mathbf{u}, p\}, \{\mathbf{w}, q\}) - F(\{\mathbf{w}, q\}) = 0, \tag{3.1}$$

where

$$\begin{aligned} B(\{\mathbf{w}, q\}, \{\mathbf{u}, p\}) = &\int_\Omega \mathbf{w} \cdot \left(\rho \frac{\partial \mathbf{u}}{\partial t} + \mathbf{u} \cdot \nabla \mathbf{u}\right) \mathrm{d}\Omega \\ &+ \int_\Omega \boldsymbol{\varepsilon}(\mathbf{w}) : \boldsymbol{\sigma}(\mathbf{u}, p) \mathrm{d}\Omega + \int_\Omega q \nabla \cdot \mathbf{u} \, \mathrm{d}\Omega \end{aligned} \tag{3.2}$$

and

$$F(\{\mathbf{w}, q\}) = \int_\Omega \mathbf{w} \cdot \rho \mathbf{f} \, \mathrm{d}\Omega + \int_{\Gamma_h} \mathbf{w} \cdot \mathbf{h} \, \mathrm{d}\Gamma. \tag{3.3}$$

Here, ρ is the fluid density, $\mathbf{f}$ is the body force per unit mass and $\mathbf{h}$ is the traction acting on the Γ_h part of the boundary Γ. The Cauchy stress $\boldsymbol{\sigma}$ is given

$$\boldsymbol{\sigma}(\mathbf{u}, p) = -p\mathbf{I} + 2\mu \, \boldsymbol{\varepsilon}(\mathbf{u}), \tag{3.4}$$

where $\mathbf{I}$, μ and $\boldsymbol{\varepsilon}(\mathbf{u})$ are the identity tensor, dynamic viscosity and the strain rate tensor, respectively, where the latter is given by

$$\boldsymbol{\varepsilon}(\mathbf{u}) = \frac{1}{2}(\nabla \mathbf{u} + \nabla \mathbf{u}^T). \tag{3.5}$$

3.2. *RBVMS and weak BCs*

At the discrete level, the fluid domain is partitioned into n_{el} subdomains Ω_e such that $\Omega = \bigcup_{e=1}^{n_{el}} \Omega^e$. Accordingly, the fluid boundary is partitioned into n_{eb} boundary elements Γ^b. We now define finite-dimensional trial and test functions as $\mathcal{S}^h \subset \mathcal{S}$ and $\mathcal{V}^h \subset \mathcal{V}$, respectively. The variational formulation of (3.1) is then stated as: Find $\{\mathbf{u}^h, p^h\} \in \mathcal{S}^h$, such that $\forall \{\mathbf{w}^h, q^h\} \in \mathcal{V}^h$

$$\begin{aligned} B(\{\mathbf{w}^h, q^h\}, \{\mathbf{u}^h, p^h\}) &+ B_{\mathrm{VMS}}(\{\mathbf{w}^h, q^h\}, \{\mathbf{u}^h, p^h\}) \\ &+ B_{\mathrm{WBC}}(\{\mathbf{w}^h, q^h\}, \{\mathbf{u}^h, p^h\}) - F(\{\mathbf{w}^h, q^h\}) = 0. \end{aligned} \tag{3.6}$$

In Eq. (3.6), B and F are given by Eqs. (3.2) and (3.3), respectively. The stabilization terms that arise from the RBVMS formulation are given by B_{VMS} as

$$\begin{aligned}
&B_{\mathrm{VMS}}(\{\mathbf{w}^h,q^h\},\{\mathbf{u}^h,p^h\})\\
&\quad=\sum_{e=1}^{n_{el}}\int_{\Omega^e}\tau_{\mathrm{SUPS}}\left(\mathbf{u}^h\cdot\nabla\mathbf{w}^h+\frac{\nabla q^h}{\rho}\right)\cdot\mathbf{r}_M(\mathbf{u}^h,p^h)\mathrm{d}\Omega\\
&\qquad+\sum_{e=1}^{n_{el}}\int_{\Omega^e}\rho\nu_{\mathrm{LSIC}}\nabla\cdot\mathbf{w}^h\mathrm{r}_C(\mathbf{u}^h)\mathrm{d}\Omega\\
&\qquad-\sum_{e=1}^{n_{el}}\int_{\Omega^e}\tau_{\mathrm{SUPS}}\,\mathbf{w}^h\cdot(\mathbf{r}_M(\mathbf{u}^h,p^h)\cdot\nabla\mathbf{u}^h)\mathrm{d}\Omega\\
&\qquad-\sum_{e=1}^{n_{el}}\int_{\Omega^e}\frac{\nabla\mathbf{w}^h}{\rho}:(\tau_{\mathrm{SUPS}}\mathbf{r}_M(\mathbf{u}^h,p^h))\otimes(\tau_{\mathrm{SUPS}}\mathbf{r}_M(\mathbf{u}^h,p^h))\mathrm{d}\Omega, \quad (3.7)
\end{aligned}$$

in which τ_{SUPS} and ν_{LSIC} are stabilization parameters that ensure stability and optimal convergence (see e.g. Refs. 102–105). In this work, we use the definitions given in Ref. 106. $\mathbf{r}_M$ and r_C are the residuals of strong form linear-momentum and continuity equations, respectively, defined as

$$\mathbf{r}_M(\boldsymbol{u}^h,p^h)=\rho\left(\frac{\partial\mathbf{u}^h}{\partial t}+\mathbf{u}\cdot\nabla\mathbf{u}^h\right)+\nabla p^h-\nabla\cdot\boldsymbol{\sigma}(\boldsymbol{u}^h,p^h) \quad (3.8)$$

and

$$\mathrm{r}_C(\boldsymbol{u}^h)=\nabla\cdot\boldsymbol{u}^h. \quad (3.9)$$

The last form, B_{WBC}, augments the terms associated with the weakly-enforced boundary conditions.[107,108,65] Given a prescribed velocity $\mathbf{g}$ on the boundary Γ_g, whose outward normal vector is denoted $\mathbf{n}$, this form reads

$$\begin{aligned}
&B_{\mathrm{WBC}}(\{\mathbf{w}^h,q^h\},\{\mathbf{u}^h,p^h\})\\
&\quad=-\sum_{b=1}^{n_{eb}}\int_{\Gamma^b\cap\Gamma_g}\mathbf{w}^h\cdot\boldsymbol{\sigma}(\mathbf{u}^h,p^h)\mathbf{n}\,\mathrm{d}\Gamma\\
&\qquad-\sum_{b=1}^{n_{eb}}\int_{\Gamma^b\cap\Gamma_g}(2\mu\,\boldsymbol{\varepsilon}(\mathbf{w}^h)\mathbf{n}+q^h\mathbf{n})\cdot(\mathbf{u}^h-\mathbf{g})\mathrm{d}\Gamma\\
&\qquad-\sum_{b=1}^{n_{eb}}\int_{\Gamma^b\cap\Gamma_g^-}\mathbf{w}^h\cdot\rho(\mathbf{u}^h\cdot\mathbf{n})(\mathbf{u}^h-\mathbf{g})\mathrm{d}\Gamma\\
&\qquad+\sum_{b=1}^{n_{eb}}\int_{\Gamma^b\cap\Gamma_g}\tau_{\mathrm{TAN}}(\mathbf{w}^h-(\mathbf{w}^h\cdot\mathbf{n})\mathbf{n})\cdot((\mathbf{u}^h-\mathbf{g})((\mathbf{u}^h-\mathbf{g})\cdot\mathbf{n})\mathbf{n})\mathrm{d}\Gamma\\
&\qquad+\sum_{b=1}^{n_{eb}}\int_{\Gamma^b\cap\Gamma_g}\tau_{\mathrm{NOR}}(\mathbf{w}^h\cdot\mathbf{n})((\mathbf{u}^h-\mathbf{g})\cdot\mathbf{n})\mathrm{d}\Gamma. \quad (3.10)
\end{aligned}$$

Here, τ_{TAN} and τ_{NOR} are boundary penalty parameters[107] in the tangential and normal directions, respectively. Γ_g^- is defined as the inflow part of Γ_g:

$$\Gamma_g^- = \{\mathbf{x} \,|\, \mathbf{u}^h \cdot \mathbf{n} < 0, \forall\, \mathbf{x} \subset \Gamma_g\}. \tag{3.11}$$

The generalized-α method[109,110,106] is employed to integrate the RBVMS equations in time.

3.3. *Turbulence-generating domain: Pressure-driven wall-bounded channel flow*

For the channel computations we characterize the flow using the friction-velocity Reynolds number, Re_τ, and the mean bulk velocity, $\overline{U}_b$. The friction-velocity Reynolds number Re_τ is given by[83]:

$$\mathrm{Re}_\tau = \frac{u^* D}{\nu}, \tag{3.12}$$

where D is the channel half-height, ν is the kinematic viscosity, and u^* is the friction velocity. The latter is given by

$$u^* = \sqrt{\nu \frac{\partial \overline{u}}{\partial n}}. \tag{3.13}$$

The non-dimensional wall distance, y^+, and velocity, u^+, are now defined as

$$y^+ = \frac{y u^*}{\nu} \tag{3.14}$$

and

$$u^+ = \frac{\overline{U}}{u^*}, \tag{3.15}$$

where y and $\overline{U}$ are the dimensional wall distance and stream-wise velocity, respectively. From Eq. (3.14) it follows that $y^+|_{\mathrm{cl}} = \mathrm{Re}_\tau$, where subscript $_{\mathrm{cl}}$ refers to the channel center line (i.e. $y = D$).

The relation between y^+ and u^+ is given by the "law of the wall", for which we use Spalding's parameterization[111] given by

$$y^+ = g(u^+) = u^+ + e^{-\chi B}\left(e^{\chi u^+} + 1 - \chi u^+ - \frac{(\chi u^+)^2}{2!} - \frac{(\chi u^+)^3}{3!}\right), \tag{3.16}$$

where $\chi = 0.4$ and $B = 5.5$.

Combining Eqs. (3.14)–(3.16), we obtain the centerline velocity as

$$\overline{U}_{\mathrm{cl}} = u^* \; u^+\big|_{\mathrm{cl}} = u^* g^{-1}(\mathrm{Re}_\tau), \tag{3.17}$$

which may be related to the mean bulk velocity by Dean's correlation[112] as

$$\overline{U}_{\mathrm{cl}} = 1.28\overline{U}_b \mathrm{Re}_b^{-0.0016}, \tag{3.18}$$

where $\mathrm{Re}_b = 2\overline{U}_b D/\nu$ is the bulk Reynolds number. The kinematic viscosity may be obtained from Eq. (3.12)

$$\nu = \frac{u^* D}{\mathrm{Re}_\tau}. \tag{3.19}$$

In addition, in a statistically-stationary flow, the mean wall shear force is balanced by the applied stream-wise pressure gradient f as

$$\int_{\Gamma_{\mathrm{ch}}} \nu \frac{\partial \overline{u}}{\partial n} \mathrm{d}\Gamma = \int_{\Omega_{\mathrm{ch}}} f \mathrm{d}\Omega. \tag{3.20}$$

A direct evaluation of the integrals in Eq. (3.20) yields

$$f = \frac{u^{*2}}{D}. \tag{3.21}$$

In practice, the relations above are incorporated in the channel-flow computations through the following initialization steps:

(1) Start with a desired $\overline{U}_b$ and Re_τ.
(2) Determine u^+ from Eq. (3.16) with $y^+ = \mathrm{Re}_\tau$.
(3) Solve for u^*, $\overline{U}_{\mathrm{cl}}$, and ν using the equation system formed by Eqs. (3.17)–(3.19).
(4) Solve for the volumetric forcing f from Eq. (3.21).

This procedure produces the *dimensional* values of the kinematic viscosity and forcing needed to carry out the channel-flow calculations at wind speeds and bridge-deck sizes corresponding to the full-scale or wind-tunnel-scale cases.

3.4. *Domain coupling and data transfer*

Projection of the velocity field from the channel outflow surface to the bridge domain inflow surface involves non-matching grids, non-conforming processor partitioning, and different element topologies, as illustrated in Fig. 2. To accommodate

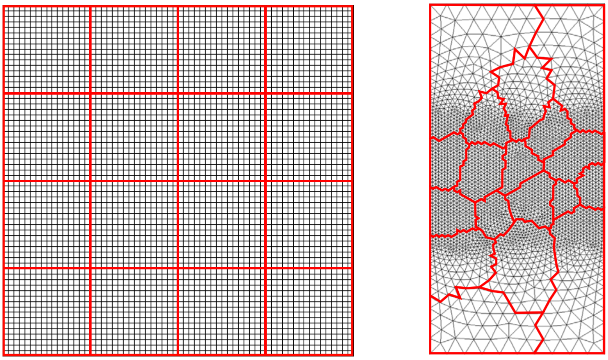

Fig. 2. Mesh and processor partitioning of the channel outflow (left) and bridge-section inflow (right).

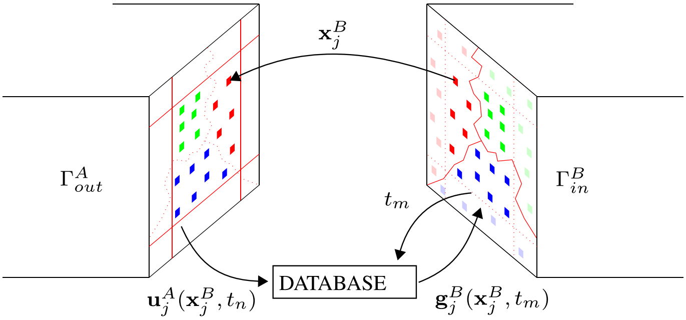

Fig. 3. Inflow velocity communication structure.

these, we present a strategy based on weakly enforced BCs, which only requires the velocity-field information at the quadrature points of the inflow of the bridge-section grid.

Following the illustration in Fig. 3, we let $\mathbf{x}_j^B$ denote the Gauss point coordinates of the bridge domain inflow surface (superscript B) associated with the local processor ID j, $j \in [1, M_{\text{proc}}]$. Next, we let $\mathbf{u}_i^A(\mathbf{x}, t)$ denote the velocity field for the channel outflow surface at time t and the local processor ID i, $i \in [1, N_{\text{proc}}]$. As an initialization step in the channel simulation we establish the connectivity between i and j, and allocate global velocity vectors associated with $\mathbf{x}_j^B$; $\mathbf{u}_j^A$. We then evaluate $\mathbf{u}_i^A(\mathbf{x}_j^B, t_n)$, where t_n is the desired time level, for all $i \cap j$, and export to global velocity vectors $\mathbf{u}_j^A(\mathbf{x}_j^B, t_n)$. Finally, we export these to a database read as part of the bridge-section simulation.

In the bridge-section domain, Eq. (3.10) governs the weak imposition of the velocity field $\mathbf{g}$ on Γ_g. As a result, at a desired time level t_m, we set $\mathbf{g}_j^B(\mathbf{x}_j^B, t_m) = \mathbf{u}_j^A(\mathbf{x}_j^B, t_m)$, determined by a linear-in-time interpolation from the neighboring time steps in the inflow velocity database as:

$$\mathbf{g}_j^B(\mathbf{x}_j^B, t_m) = (1-\xi)\mathbf{u}_j^A(\mathbf{x}_j^B, t_n) + \xi \mathbf{u}_j^A(\mathbf{x}_j^B, t_{n+1}), \tag{3.22}$$

$$t_m = (1-\xi)t_n + \xi t_{n+1}, \quad t_n < t_m < t_{n+1}. \tag{3.23}$$

In addition, because the flow is incompressible, we ensure that the flow rate at the inlet remains constant and consistent with the set bulk velocity $\overline{U}_b$, by explicitly enforcing the following condition on the inflow velocity at each time level:

$$\int_{\Gamma_g} (\mathbf{g} \cdot \mathbf{n} - \overline{U}_b) \mathrm{d}\Gamma = 0. \tag{3.24}$$

Remark. The data projection approach presented here is very similar to that described in Ref. 79. However, in the present work, the step where the velocity is projected onto the inlet nodal space is not needed since the quadrature-point values are used directly in the enforcement of weak BCs.

4. IGA Simulations of Turbulent Channel Flows

The channel height is set to 2 m, which is the vertical dimension of the wind tunnel described in the authors' earlier work.[21,78] At the walls, no-slip BCs are enforced weakly and no-penetration BCs are enforced strongly. The channel stream-wise and span-wise dimensions are 6 m and 2 m, respectively. Periodic BCs are applied in these directions. The bulk velocity is set to $\overline{U}_b = 2.0\,\text{m/s}$, and Re_τ of 395 and 2000 are considered in this work.

For the discretization, we use C^1-continuous quadratic NURBS and a uniform mesh of $192 \times 64 \times 64$ elements. It should be noted that the smallest length scales resolved for the given mesh then becomes approximately 30 mm, or $B/16$. The domain is partitioned into $16 \times 4 \times 4$ processors and the time step is set to $\Delta t = 0.01\,\text{s}$.

The simulations are carried out until a statistically stationary flow is achieved. The flow patterns in this state are depicted in Fig. 4, showing instantaneous vertical velocity contours for a channel cross-section for both Reynolds numbers. For $\text{Re}_\tau = 395$ and $\text{Re}_\tau = 2000$, the turbulence intensities are approximately 4.4% and 2.9%, respectively. The mean stream-wise velocity and root mean square (RMS) of the velocity fluctuations are shown in Figs. 5 and 6, respectively. For $\text{Re}_\tau = 395$ both the mean and RMS profiles match the DNS results very well. For $\text{Re}_\tau = 2000$, while the mean velocity is very accurate, we see more deviation in RMS profile. However, considering that the first knot is located at $y^+ = 63$, the results are very good, and underscore the effectiveness and accuracy of RBVMS and weak BCs discretized with NURBS for this problem class.

Figure 7 shows the vertical versus longitudinal velocity fluctuations at the channel centerline. The uncorrelated fluctuations reveal an isotropic turbulence field in the channel center, which is the flow that will be directly impacting the bridge deck. Velocity spectra for the stream-wise (u) and span-wise (w) velocity components are

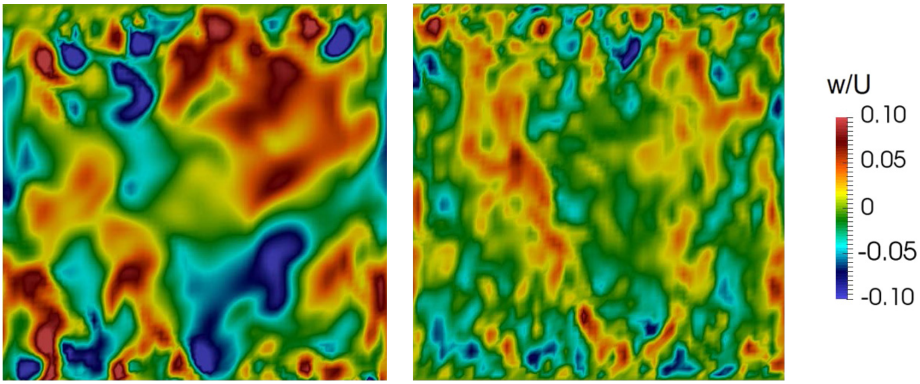

(a) $\text{Re}_\tau = 395$ (b) $\text{Re}_\tau = 2000$

Fig. 4. Instantaneous span-wise velocity contours plotted on a channel cross-section.

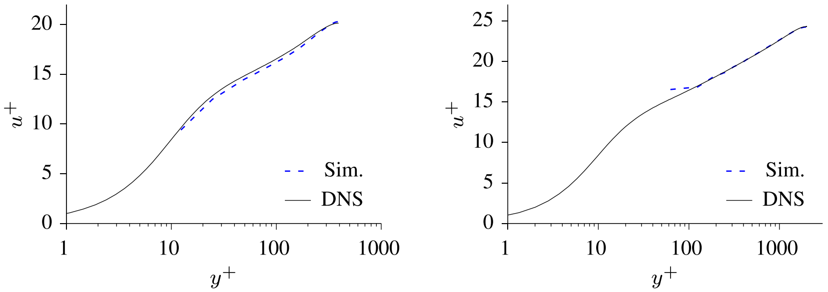

(a) $\mathrm{Re}_\tau = 395$, DNS data from Ref. 113. (b) $\mathrm{Re}_\tau = 2000$, DNS data from Ref. 114.

Fig. 5. Mean stream-wise velocity in nondimensional units for the channel-flow simulations.

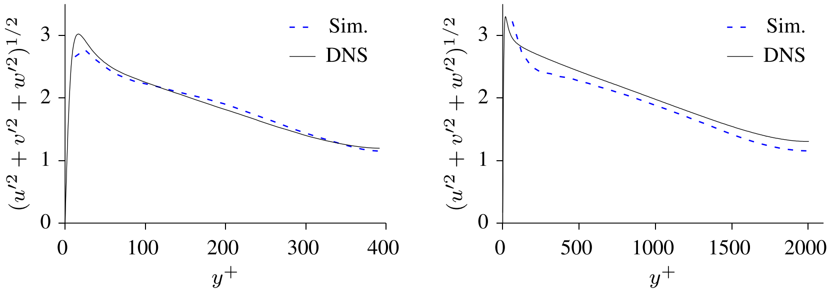

(a) $\mathrm{Re}_\tau = 395$, DNS data from Ref. 113. (b) $\mathrm{Re}_\tau = 2000$, DNS data from Ref. 114.

Fig. 6. RMS of velocity fluctuations in nondimensional units for the channel-flow simulations.

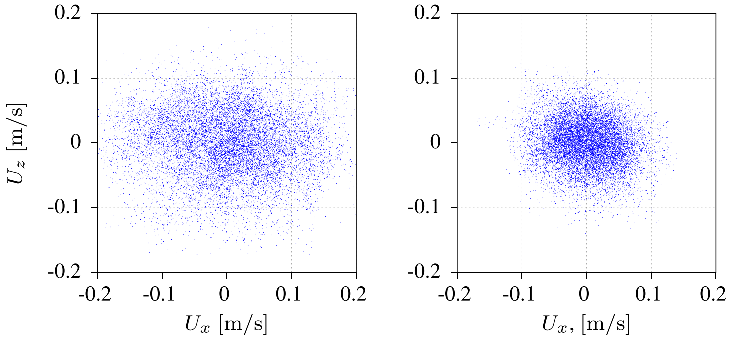

Fig. 7. Scatter plot of the stream-wise and span-wise velocity fluctuations at the channel centerline. Left: $\mathrm{Re}_\tau = 395$; Right: $\mathrm{Re}_\tau = 2000$.

shown in Figs. 8 and 9, respectively. The velocities were sampled at a fixed spatial point for a 50 s period. The same plots also show the least-squares fitted curves of the classical von Kármán one-point spectra,[115] which for the u and w component can be written on the following form[116]:

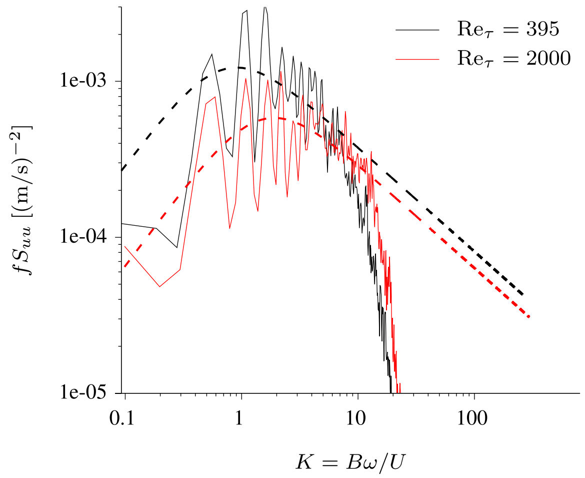

Fig. 8. Spectra of the stream-wise velocity fluctuations for $\mathrm{Re}_\tau = 395$ and $\mathrm{Re}_\tau = 2000$ with von Kármán fitting.

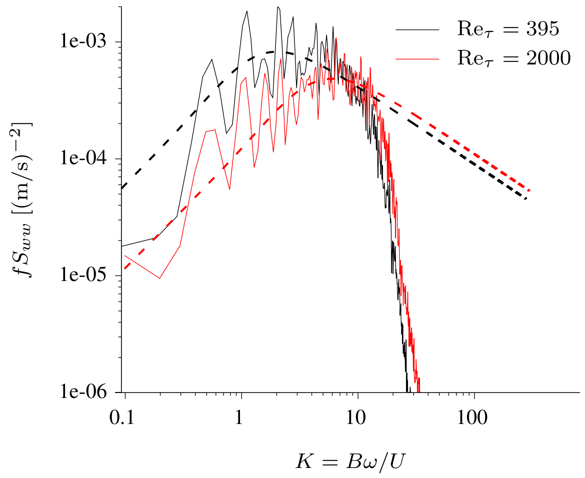

Fig. 9. Spectra of the span-wise velocity fluctuations for $\mathrm{Re}_\tau = 395$ and $\mathrm{Re}_\tau = 2000$ with von Kármán fitting.

$$\frac{fS_{uu}(f)}{\sigma_u^2} = \frac{4f_u}{(1 + 70.8f_u^2)^{5/6}}, \tag{4.1}$$

and

$$\frac{fS_{ww}(f)}{\sigma_w^2} = \frac{4f_w(1 + 755.2f_w^2)}{(1 + 283.2f_w^2)^{11/6}}. \tag{4.2}$$

Here, f is the frequency, $\sigma_i, i = \{u, w\}$ is the variance of $i(t)$ and $f_i = f\,{}^xL_i/U$ where ${}^xL_i$ is the characteristic length scale of the ith component. The spectra show good correspondence to the Kolmogorov energy cascade and also follow the

$-5/3$ slope of the inertial subrange in the range of resolved scales. It is also clear that RBVMS, unlike pure Galerkin methods, provides effective dissipation at high frequencies.

Remark 4.1. We emphasize that the state of isotropic turbulence is only expected in the channel core.

Remark 4.2. Because the cutoff frequency is inversely proportional to the mesh element size, the cost for resolving higher frequencies increase rapidly. The channel flow computations were set up with buffeting forces in mind, for which the current frequency content is in the range of interest.

5. FEM Simulations of the Bridge Section

In this section, we report the results of the simulations of the rectangular bridge section subjected to the wind fields presented in Sec. 4. We also carry out a simulation using a uniform inflow BCs for comparison.

5.1. *Problem setup*

The computational setup for this case consists of a bridge sectional model that is centered between the walls that mimic those of the wind tunnel. For the cross-section, we consider a simple rectangular cylinder with aspect ratio 1:10, shown in Fig. 1, with physical dimensions of $0.5 \times 0.05\,\mathrm{m}$. The section is referred to as “BD10”. The inflow surface is placed 2.5 B upwind and the outflow surface is placed 6 B downwind from the section centroid. The domain width is set to 1.0 m and the section width is that of the entire domain.

The simulations make use of linear tetrahedra. To resolve the incoming turbulence a refinement region that extends from the inlet and 3 B downwind from the section is defined. A smaller refinement region around the shear layers is also introduced. At the section's surface, four layers of prismatic boundary-layer elements of thickness 0.3 mm are constructed. In total, the mesh has 1.2 M nodes and 6.4 M elements. The mesh is partitioned into 512 subdomains using METIS,[117] and each subdomain is assigned a compute core.

The boundary conditions are defined as follows. At the walls, no-slip BC is enforced weakly, as a continuation of the channel computation. The outlet is set to have a zero traction BC, and, at the lateral boundaries, no-penetration BCs are adopted. Weakly-enforced no slip and no-penetration BCs are set at the bridge-section surface. At the inlet, velocity field from the channel flow simulation is imposed weakly. Fluid properties of air, with density $\rho = 1.225\,\mathrm{kg/m^3}$ and dynamic viscosity $\mu = 1.848 \times 10^{-5}\,\mathrm{kg/ms}$, are employed in the bridge section simulations. The time step is set to $\Delta t = 1 \times 10^{-4}\,\mathrm{s}$ for all cases.

The aerodynamic forces and pressures are integrated at seven strips of 10 mm width. The strips are positioned such that we obtain span-wise distances of $nB/50$,

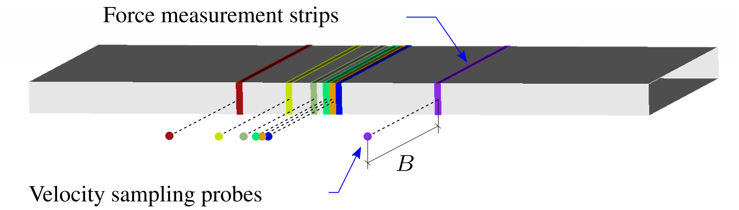

Fig. 10. Velocity and force sampling layout.

$n = \{1, 2, 4, 8, 16, 32\}$, as shown int Fig. 10. The strips are centered in the domain as to eliminate any effects that arise from the span-wise boundary conditions. A sufficiently narrow force measurement strips were chosen so that the buffeting forces can be assumed fully correlated, and the span-wise coherence can be set to unity. The corresponding velocity sampling points were placed at a distance B upwind of the bridge-section leading edge.

5.2. *Buffeting and aerodynamic admittance results*

The $\mathrm{Re}_\tau = 395$ and $\mathrm{Re}_\tau = 2000$, with $\overline{U}_b = 2\,\mathrm{m/s}$, are simulated for $50\,\mathrm{s}$, of which we discard the first $2.5\,\mathrm{s}$ to let the flow fully develop. A $5\,\mathrm{s}$ window of the drag and lift coefficients for the force measuring strip located in the middle of the section is

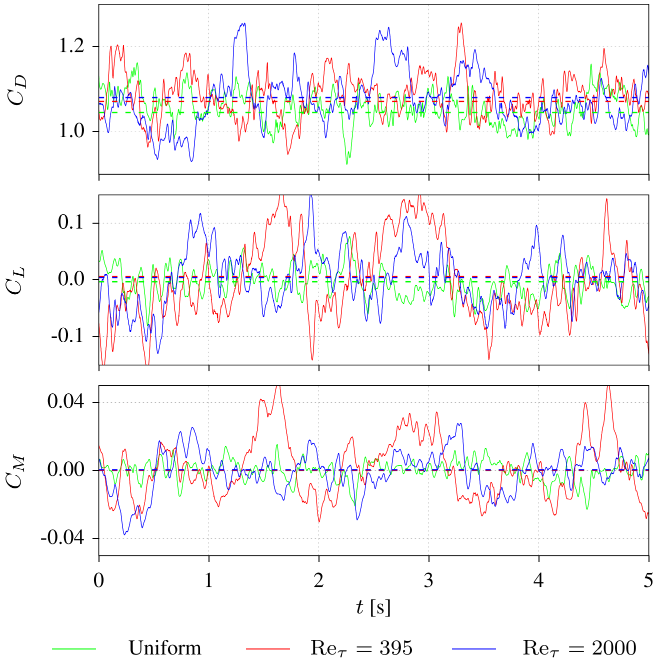

Fig. 11. Time series of the drag and lift coefficients for $\mathrm{Re}_\tau = 395$, $\mathrm{Re}_\tau = 2000$, and uniform inflow. The dashed lines correspond to the mean values.

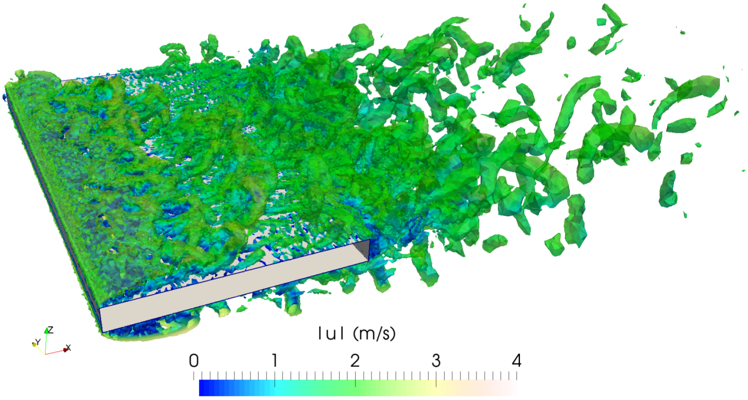

(a) Turbulent inflow corresponding to $\mathrm{Re}_\tau = 395$.

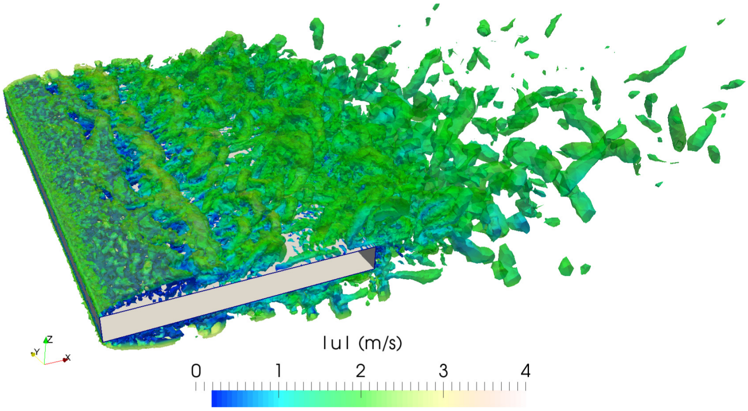

(b) Uniform inflow.

Fig. 12. Isosurfaces of the vorticity colored by flow speed.

shown in Fig. 11. Visualization of the flow for the $\mathrm{Re}_\tau = 395$ and uniform-inflow simulations are shown in Fig. 12.

The time series give a good first impression of the effect of incident turbulence. First of all, we notice that besides the vortex shedding frequency there is an additional, and more irregular component that we recognize as a buffeting force. The time series further suggests that the buffeting components of lift and pitching moment are highly correlated, and seemingly independent of the turbulence-induced drag, which speaks in favor of the auto-spectral assumption of buffeting forces (see Eq. (2.6)). Finally, we note that the average drag coefficient increases from approximately 1.05 to 1.08 when the bridge section is subjected to turbulent flow. The turbulent wakes shown in Fig. 12 further prove the irregularity that incident turbulence triggers. We clearly see that the vortices are almost fully correlated for uniform inflow, they have a much more 3D and random character for the turbulent inflow case.

The spectra for the drag, lift and pitching moment, averaged over the measurement strips, are shown in Fig. 13. The buffeting is recognized as the differences between the curves of turbulent and uniform inflow, which do reflect the velocity spectra well (Figs. 8 and 9), limited by the domain size at the lower end ($K \approx 0.4$) and the mesh density as the upper limit ($K \approx 15$). We further see that, at higher frequencies, the force spectra are equal for all inflow conditions and recognize

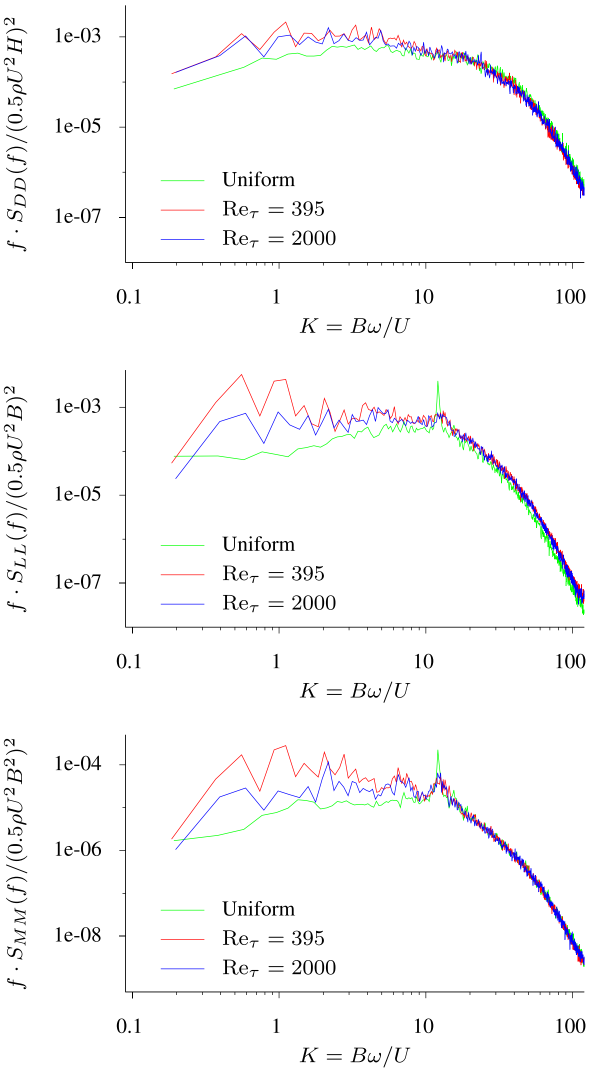

Fig. 13. Normalized spectra of the drag, lift and pitching moment for uniform inflow, $\mathrm{Re}_\tau = 395$ and 2000.

this as the "signature turbulence" of the bridge. The vortex shedding frequency ($K = 12.1 \Rightarrow St = 0.192$), which contains almost all the energy of the uniform inflow, is hardly notable for the turbulent cases. This observation is supported by Fig. 12, and also clearly demonstrates the well-known fact that turbulence disturbs the vortex formation and no regular shedding is seen.[86]

We now use the velocity and force spectra to identify the aerodynamic admittance functions by Eq. (2.6). The results are shown in Fig. 14. For comparison, we have also plotted the Sears function given by Eq. (2.7), which represents the airfoil solution for lift admittance. The drag coefficient was set to $\bar{C}_D = 1.05$, taken from

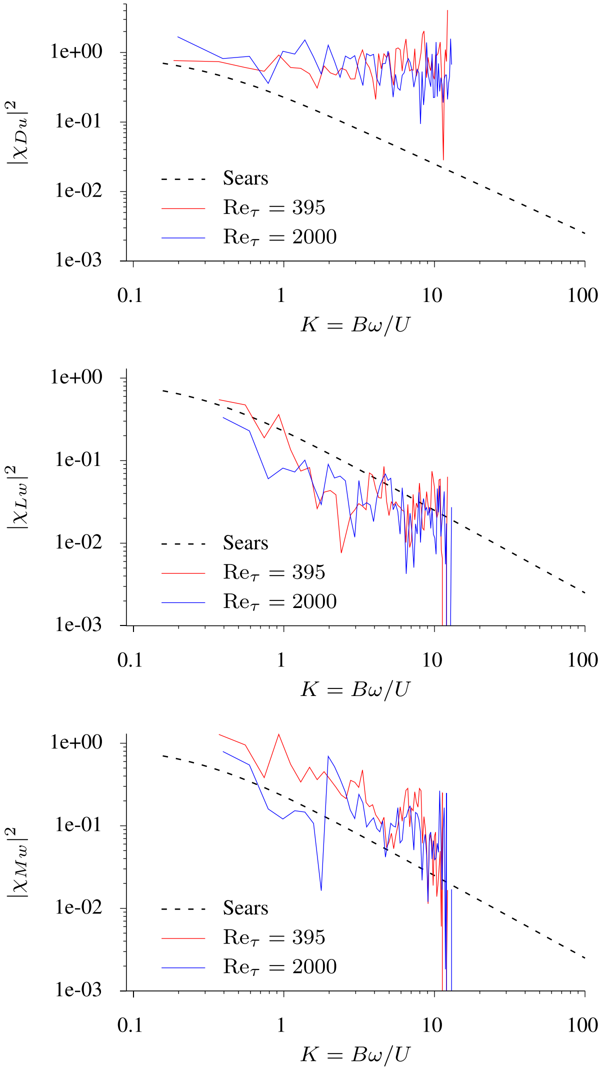

Fig. 14. Aerodynamic admittance functions.

the uniform inflow time series, and the slope of the lift and pitching moments were set to $C'_L = 8.60$ and $C'_M = 1.089$, respectively. The latter were determined through wind tunnel experiments as a part of our previous work.[21]

By utilizing the essential property of linearity in the frequency domain,[118] we isolate the buffeting action by subtracting the uniform spectra from the turbulent ones. This effect is negligible for lower frequencies, but makes a significant difference when approaching the vortex shedding frequency. It should be remarked that the validity of the computed admittance functions relies on sufficient frequency content of the velocity spectra, which, in our case, corresponds to the range of $K \approx 0.4$ to 15.

The computed admittance functions suffer from relatively low resolution due to limited duration of the time series, which is a limitation for numerical simulations in general. Nevertheless, we still capture the admittance properties of the bridge deck. For the drag, we see that the admittance has a constant value of unity, i.e. the horizontal velocity fluctuations are directly transferred to the drag forces as in the quasi-steady theory. For the admittances associated with lift and pitching moment, however, we see that they exhibit the same asymptotic behavior as the Sears function. The lift has a slightly lower magnitude, which is consistent with the observations reported in Ref. 10 where the same section was studied. For the pitching moment, which lies above the Sears function, the section seems to receive full admittance to a certain level before it decays. The computed admittance functions generally confirm that the BD10 section exhibits very similar buffeting response to that of an airfoil.

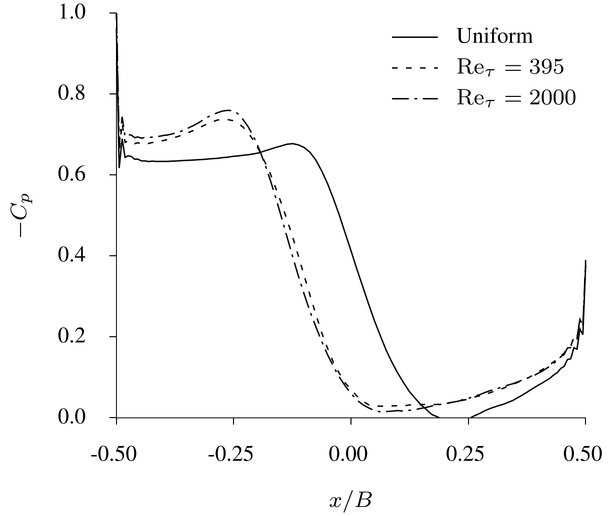

Fig. 15. Time-averaged pressure coefficient on a surface of the BD10 section for different flow conditions.

5.3. *Temporal statistics*

In this section, we study the impact of incident turbulence on the time-averaged flow characteristics. The data are sampled from $t = 15\,\mathrm{s}$ to $t = 20\,\mathrm{s}$ with a sampling frequency of $0.1\,\mathrm{s}$. The pressure, reported in terms of the pressure coefficient $C_p = p/(1/2\rho\overline{U}_b^2)$, is averaged in the span-wise direction over 75% of the span in order to eliminate boundary-condition effects at the bridge-section edges.

Figures 15 and 16 show the time-averaged pressure coefficient and velocity contours, respectively, for the uniform and turbulent inflow cases. It is clear from

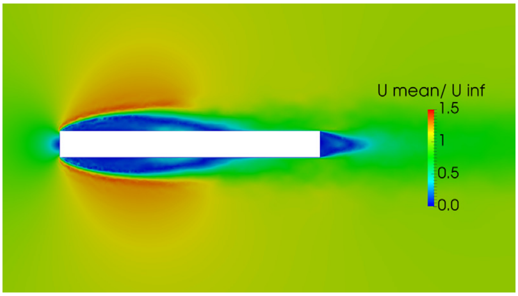

(a) Uniform

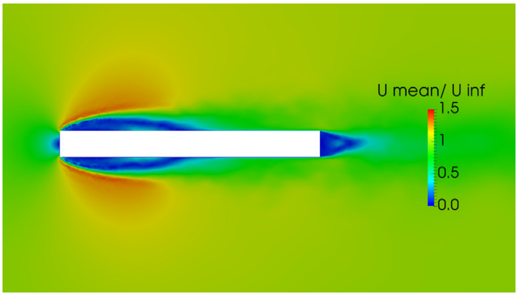

(b) $\mathrm{Re}_\tau = 395$

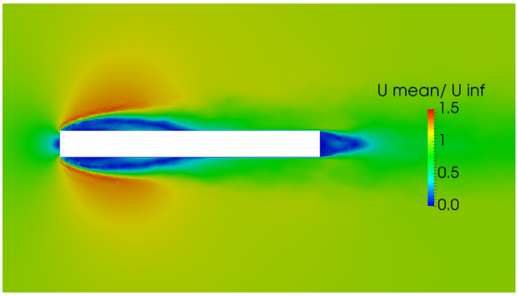

(c) $\mathrm{Re}_\tau = 2000$

Fig. 16. Contours of time-averaged flow velocity divided by $\overline{U}_b$ for different flow conditions.

the figures that turbulence in the flow makes the reattachment length significantly lower. In addition, the peak base suction increases near the leading edge. This observation was also made experimentally for the same section in Ref. 86, where the authors explained the increased base suction with the shorter vortex formation length and thereby increased shedding of the vortices. The results are also consistent with a drastic reduction of the separation bubble for turbulent inflow around a sphere shown in Ref. 82. We further note that the pressure profiles for the two turbulence intensities are very similar. This suggests that the vortex formation depends as much on the presence of disturbances in the incoming flow, as the intensity or scales of the turbulence. These observations may be of significant interest for CFD applications that use experimental results for validation, in that classical assumption of uniform inflow may overestimate the reattachment length. For nonzero angle of attack, or non-symmetrical sections, this effect gives an overestimation of the lift and pitching moment, which is a general, but not yet explained, result in many numerical simulation of bridges (see e.g. Refs. 119, 19, 21 and 25).

6. Conclusions

A framework to carry out buffeting analysis of bridge sections is presented. The framework makes use the RBVMS formulation of the Navier–Stokes equations of incompressible flows, weakly enforced BCs, and an MDM approach that couples a turbulent inflow generation domain with a domain for the analysis of the bridge section. Coupling between the two domains makes use of weak BCs as a core technology, and naturally enables different discretizations in both subdomains. The turbulence-generating domain makes use of a pressure-driven channels flow setup, where the turbulent flow, and, in particular, the turbulence intensity, is controlled using the bulk velocity and friction-velocity-based Reynolds number. The channel simulations produced highly isotropic and realistic velocity spectra in the channel core with effective high-frequency dissipation. This accuracy was achieved due to the use of RBVMS, weak BCs, and a discretization using NURBS-based IGA. To illustrate the modularity of the framework, the bridge section was simulated using RBVMS and weak BCs, but discretized using traditional low-order FEM.

From the aerodynamic forces on the bridge section we separated buffeting from vortex shedding and signature turbulence by subtracting the uniform-inflow force spectra. The resulting aerodynamic admittance functions for the lift and pitching moment were shown to exhibit a buffeting response that follows the Sears analytical solution for airfoils.[2] It was further shown that incident turbulence had a significant effect on the flow patterns around the bridge section. As observed earlier in Refs. 86 and 82, under turbulent inflow, the separation-bubble reattachment length was reduced, which, in turn, gave rise to a pressure profile that differs significantly from the uniform-inflow case. Because the averaged drag, flow velocity, and pressure coefficient are very similar for two different values of Re_τ, we hypothesize that these quantities are more dependent on the presence of ambient turbulence than on the details of turbulent structures. This statement, however, needs further investigation. Nevertheless, these observations explain why numerical simulations of bluff body aerodynamics using uniform inflow generally overestimate the magnitudes of lift and pitching moment.

Acknowledgments

This work was carried out with financial support from the Norwegian Public Roads Administration. YB was partially supported by the NSF Award No. 1854436. All simulations were performed using resources provided by UNINETT Sigma2 – the National Infrastructure for High Performance Computing and Data Storage in Norway. TAH was partially funded by Dr. Techn. Olav Olsen AS. The authors greatly acknowledge this support.

References

1. H. G. Küssner, Zusammenfassender Bericht über den instationären Auftrieb von Flügeln, *Luftfahrtforschung* **13** (1936) 410–424.
2. W. R. Sears, Some aspects of non-stationary airfoil theory and its practical application, *J. Aeronaut. Sci.* **8** (1941) 104–108.
3. A. G. Davenport, Buffeting of a suspension bridge by storm winds, *J. Struct. Div.* **88** (1962) 233–270.
4. X. Chen, M. Matsumoto and A. Kareem, Aerodynamic coupling effects on flutter and buffeting of bridges, *J. Eng. Mech.* **126** (2000) 17–26.
5. A. Jain, N. P. Jones and R. H. Scanlan, Coupled flutter and buffeting analysis of long-span bridges, *J. Struct. Eng.* **122** (1996) 716–725.
6. R. H. Scanlan, The action of flexible bridges under wind, II: Buffeting theory, *J. Sound Vib.* **60** (1978) 201–211.
7. L. D. Zhu and Y. L. Xu, Buffeting response of long-span cable-supported bridges under skew winds. Part 1: Theory, *J. Sound Vib.* **281** (2005) 647–673.
8. X. Chen, M. Matsumoto and A. Kareem, Time domain flutter and buffeting response analysis of bridges, *J. Eng. Mech.* **126** (2000) 7–16.
9. G. Diana, G. Fiammenghi, M. Belloli and D. Rocchi, Wind tunnel tests and numerical approach for long span bridges: The Messina bridge, *J. Wind Eng. Indust. Aerodyn.* **122** (2013) 38–49.
10. E. D. Jancauskas and W. H. Melbourne, The aerodynamic admittance of two-dimensional rectangular section cylinders in smooth flow, *J. Wind Eng. Indust. Aerodyn.* **23** (1986) 395–408.
11. G. L. Larose, Experimental determination of the aerodynamic admittance of a bridge deck segment, *J. Fluids Struct.* **13** (1999) 1029–1040.
12. G. L. Larose and J. Mann, Gust loading on streamlined bridge decks, *J. Fluids Struct.* **12** (1998) 511–536.
13. R. Sankaran and E. D. Jancauskas, Direct measurement of the aerodynamic admittance of two-dimensional rectangular cylinders in smooth and turbulent flows, *J. Wind Eng. Indust. Aerodyn.* **41** (1992) 601–611.
14. D. E. Walshe and T. A. Wyatt, Measurement and application of the aerodynamic admittance function for a box-girder bridge, *J. Wind Eng. Indust. Aerodyn.* **14** (1983) 211–222.

15. L. Yan, L. D. Zhu and R. G. J. Flay, Identification of aerodynamic admittance functions of a flat closed-box deck in different grid-generated turbulent wind fields, *Adv. Struct. Eng.* **21** (2018) 380–395.
16. G. L. Larose, H. Tanaka, N. J. Gimsing and C. Dyrbye, Direct measurements of buffeting wind forces on bridge decks, *J. Wind Eng. Indust. Aerodyn.* **74**–**76** (1998) 809–818.
17. S. Li, M. Li and G. L. Larose, Aerodynamic admittance of streamlined bridge decks, *J. Fluids Struct.* **78** (2018) 1–23.
18. Y. Bai, D. Sun and J. Lin, Three dimensional numerical simulations of long-span bridge aerodynamics, using block-iterative coupling and DES, *Comput. Fluids* **39** (2010) 1549–1561.
19. S. de Miranda, L. Patruno, F. Ubertini and G. Vairo, On the identification of flutter derivatives of bridge decks via RANS turbulence models: Benchmarking on rectangular prisms, *Eng. Struct.* **76** (2014) 359–370.
20. J. B. Frandsen, Numerical bridge deck studies using finite elements. Part I: Flutter, *J. Fluids Struct.* **19** (2004) 171–191.
21. T. A. Helgedagsrud, Y. Bazilevs, A. Korobenko, K. M. Mathisen and O. A. Øiseth, Using ALE-VMS to compute aerodynamic derivatives of bridge sections, *Comput. Fluids* (2018), doi:10.1016/j.compfluid.2018.04.037.
22. A. Larsen and J. H. Walther, Discrete vortex simulation of flow around five generic bridge deck sections, *J. Wind Eng. Indust. Aerodyn.* **77**–**78** (1998) 591–602.
23. A. Šarkić, R. Fisch, R. Höffer and K. U. Bletzinger, Bridge flutter derivatives based on computed, validated pressure fields, *J. Wind Eng. Indust. Aerodyn.* **104**–**106** (2012) 141–151.
24. M. W. Sarwar, T. Ishihara, K. Shimada, Y. Yamasaki and T. Ikeda, Prediction of aerodynamic characteristics of a box girder bridge section using the LES turbulence model, *J. Wind Eng. Indust. Aerodyn.* **96** (2008) 1895–1911.
25. R. Scotta, M. Lazzari, E. Stecca, J. Cotela and R. Rossi, Numerical wind tunnel for aerodynamic and aeroelastic characterization of bridge deck sections, *Comput. Struct.* **167** (2016) 96–114.
26. M. M. Hejlesen, J. T. Rasmussen, A. Larsen and J. H. Walther, On estimating the aerodynamic admittance of bridge sections by a mesh-free vortex method, *J. Wind Eng. Indust. Aerodyn.* **146** (2015) 117–127.
27. J. T. Rasmussen, M. M. Hejlesen, A. Larsen and J. H. Walther, Discrete vortex method simulations of the aerodynamic admittance in bridge aerodynamics, *J. Wind Eng. Indust. Aerodyn.* **98** (2010) 754–766.
28. Y. Bazilevs, V. M. Calo, J. A. Cottrell, T. J. R. Hughes, A. Reali and G. Scovazzi, Variational multiscale residual-based turbulence modeling for large eddy simulation of incompressible flows, *Comput. Methods Appl. Mech. Eng.* **197** (2007) 173–201.
29. Y. Bazilevs and I. Akkerman, Large eddy simulation of turbulent Taylor–Couette flow using isogeometric analysis and the residual-based variational multiscale method, *J. Comput. Phys.* **229** (2010) 3402–3414.
30. Y. Bazilevs, M.-C. Hsu, K. Takizawa and T. E. Tezduyar, ALE-VMS and ST-VMS methods for computer modeling of wind-turbine rotor aerodynamics and fluid-structure interaction, *Math. Models Methods Appl. Sci.* **22** (2012) 1230002.
31. Y. Bazilevs, K. Takizawa and T. E. Tezduyar, Challenges and directions in computational fluid–structure interaction, *Math. Models Methods Appl. Sci.* **23** (2013) 215–221.

32. Y. Bazilevs, K. Takizawa and T. E. Tezduyar, New directions and challenging computations in fluid dynamics modeling with stabilized and multiscale methods, *Math. Models Methods Appl. Sci.* **25** (2015) 2217–2226.
33. J. Yan, A. Korobenko, A. E. Tejada-Martínez, R. Golshan and Y. Bazilevs, A new variational multiscale formulation for stratified incompressible turbulent flows, *Comput. Fluids* **158** (2017) 150–156.
34. T. M. van Opstal, J. Yan, C. Coley, J. A. Evans, T. Kvamsdal, and Y. Bazilevs, Isogeometric divergence-conforming variational multiscale formulation of incompressible turbulent flows, *Comput. Methods Appl. Mech. Eng.* **316** (2017) 859–879.
35. J. Yan, S. Lin, Y. Bazilevs and G. J. Wagner, Isogeometric analysis of multi-phase flows with surface tension and with application to dynamics of rising bubbles, *Comput. Fluids* (2018), doi:10.1016/j.compfluid.2018.04.017.
36. K. Takizawa and T. E. Tezduyar, Multiscale space–time fluid–structure interaction techniques, *Comput. Mech.* **48** (2011) 247–267.
37. K. Takizawa and T. E. Tezduyar, Space–time fluid–structure interaction methods, *Math. Models Methods Appl. Sci.* **22** (2012) 1230001.
38. K. Takizawa, Y. Bazilevs, T. E. Tezduyar, Ming-Chen Hsu, O. Øiseth, K. M. Mathisen, N. Kostov and S. McIntyre, Engineering analysis and design with ALE-VMS and space–time methods, *Arch. Comput. Methods Eng.* **21** (2014) 481–508.
39. K. Takizawa, Computational engineering analysis with the new-generation space–time methods, *Comput. Mech.* **54** (2014) 193–211.
40. K. Takizawa, T. E. Tezduyar, H. Mochizuki, H. Hattori, S. Mei, L. Pan and K. Montel, Space–time VMS method for flow computations with slip interfaces (ST-SI), *Math. Models Methods Appl. Sci.* **25** (2015) 2377–2406.
41. K. Takizawa and T. E. Tezduyar, New directions in space–time computational methods, in *Advances in Computational Fluid–Structure Interaction and Flow Simulation*: *New Methods and Challenging Computations*, eds. Y. Bazilevs and K. Takizawa, Modeling and Simulation in Science, Engineering and Technology (Springer, 2016), pp. 159–178.
42. K. Takizawa, T. E. Tezduyar, J. Boben, N. Kostov, C. Boswell and A. Buscher, Fluid–structure interaction modeling of clusters of spacecraft parachutes with modified geometric porosity, *Comput. Mech.* **52** (2013) 1351–1364.
43. K. Takizawa, T. E. Tezduyar, C. Boswell, Y. Tsutsui and K. Montel, Special methods for aerodynamic-moment calculations from parachute FSI modeling, *Comput. Mech.* **55** (2015) 1059–1069.
44. K. Takizawa, T. E. Tezduyar, C. Boswell, R. Kolesar and K. Montel, FSI modeling of the reefed stages and disreefing of the Orion spacecraft parachutes, *Comput. Mech.* **54** (2014) 1203–1220.
45. K. Takizawa, T. E. Tezduyar, R. Kolesar, C. Boswell, T. Kanai and K. Montel, Multiscale methods for gore curvature calculations from FSI modeling of spacecraft parachutes, *Comput. Mech.* **54** (2014) 1461–1476.
46. K. Takizawa, T. E. Tezduyar and R. Kolesar, FSI modeling of the Orion spacecraft drogue parachutes, *Comput. Mech.* **55** (2015) 1167–1179.
47. K. Takizawa, T. E. Tezduyar and T. Terahara, Ram-air parachute structural and fluid mechanics computations with the space–time isogeometric analysis (ST-IGA), *Comput. Fluids* **141** (2016) 191–200.
48. K. Takizawa, T. E. Tezduyar and T. Kanai, Porosity models and computational methods for compressible-flow aerodynamics of parachutes with geometric porosity, *Math. Models Methods Appl. Sci.* **27** (2017) 771–806.
49. T. Kanai, K. Takizawa, T. E. Tezduyar, T. Tanaka and A. Hartmann, Compressible-flow geometric-porosity modeling and spacecraft parachute computation with

isogeometric discretization, *Comput. Mech.* published online (2018), doi:10.1007/s00466-018-1595-4.

50. K. Takizawa, T. E. Tezduyar and H. Hattori, Computational analysis of flow-driven string dynamics in turbomachinery, *Comput. Fluids* **142** (2017) 109–117.
51. K. Takizawa, T. E. Tezduyar, Y. Otoguro, T. Terahara, T. Kuraishi and H. Hattori, Turbocharger flow computations with the space–time isogeometric analysis (ST-IGA), *Comput. Fluids* **142** (2017) 15–20.
52. Y. Otoguro, K. Takizawa and T. E. Tezduyar, Space–time VMS computational flow analysis with isogeometric discretization and a general-purpose NURBS mesh generation method, *Comput. Fluids* **158** (2017) 189–200.
53. Y. Otoguro, K. Takizawa and T. E. Tezduyar, A general-purpose NURBS mesh generation method for complex geometries, in *Frontiers in Computational Fluid–Structure Interaction and Flow Simulation*: *Research from Lead Investigators Under Forty – 2018*, ed. T. E. Tezduyar, Modeling and Simulation in Science, Engineering and Technology (Springer, 2018), pp. 399–434.
54. Y. Otoguro, K. Takizawa, T. E. Tezduyar, K. Nagaoka and S. Mei, Turbocharger turbine and exhaust manifold flow computation with the space–time variational multiscale method and isogeometric analysis, *Comput. Fluids* published online (2018), doi:10.1016/j.compfluid.2018.05.019.
55. K. Takizawa, T. E. Tezduyar and T. Kuraishi, Multiscale ST methods for thermo-fluid analysis of a ground vehicle and its tires, *Math. Models Methods Appl. Sci.* **25** (2015) 2227–2255.
56. K. Takizawa, T. E. Tezduyar, T. Kuraishi, S. Tabata and H. Takagi, Computational thermo-fluid analysis of a disk brake, *Comput. Mech.* **57** (2016) 965–977.
57. K. Takizawa, T. E. Tezduyar, A. Buscher and S. Asada, Space–time interface-tracking with topology change (ST-TC), *Comput. Mech.* **54** (2014) 955–971.
58. K. Takizawa, T. E. Tezduyar, A. Buscher and S. Asada, Space–time fluid mechanics computation of heart valve models, *Comput. Mech.* **54** (2014) 973–986.
59. K. Takizawa, T. E. Tezduyar and A. Buscher, Space–time computational analysis of MAV flapping-wing aerodynamics with wing clapping, *Comput. Mech.* **55** (2015) 1131–1141.
60. K. Takizawa, T. E. Tezduyar, S. Asada and T. Kuraishi, Space–time method for flow computations with slip interfaces and topology changes (ST-SI-TC), *Comput. Fluids* **141** (2016) 124–134.
61. K. Takizawa, T. E. Tezduyar, T. Terahara and T. Sasaki, Heart valve flow computation with the space–time slip interface topology change (ST-SI-TC) method and isogeometric analysis (IGA), in *Biomedical Technology*: *Modeling*, *Experiments and Simulation*, eds. P. Wriggers and T. Lenarz, Lecture Notes in Applied and Computational Mechanics (Springer, 2018), pp. 77–99.
62. K. Takizawa, T. E. Tezduyar, T. Terahara and T. Sasaki, Heart valve flow computation with the integrated space–time VMS, slip interface, topology change and isogeometric discretization methods, *Comput. Fluids* **158** (2017) 176–188.
63. T. Kuraishi, K. Takizawa and T. E. Tezduyar, Space–time computational analysis of tire aerodynamics with actual geometry, road contact and tire deformation, in *Frontiers in Computational Fluid–Structure Interaction and Flow Simulation*: *Research from Lead Investigators Under Forty – 2018*, ed. T. E. Tezduyar, Modeling and Simulation in Science, Engineering and Technology (Springer, 2018), pp. 337–376.
64. T. Kuraishi, K. Takizawa and T. E. Tezduyar, Tire aerodynamics with actual tire geometry, road contact and tire deformation, *Comput. Mech.* published online (2018), doi:10.1007/s00466-018-1642-1.

65. Y. Bazilevs, C. Michler, V. M. Calo and T. J. R. Hughes, Isogeometric variational multiscale modeling of wall-bounded turbulent flows with weakly enforced boundary conditions on unstretched meshes, *Comput. Methods Appl. Mech. Eng.* **199** (2010) 780–790.
66. M.-C. Hsu, I. Akkerman and Y. Bazilevs, Wind turbine aerodynamics using ALE–VMS: Validation and the role of weakly enforced boundary conditions, *Comput. Mech.* **50** (2012) 499–511.
67. J. Yan, A. Korobenko, X. Deng and Y. Bazilevs, Computational free-surface fluid–structure interaction with application to floating offshore wind turbines, *Comput. Fluids* **141** (2016) 155–174.
68. A. Korobenko, J. Yan, S. M. I. Gohari, S. Sarkar and Y. Bazilevs, FSI simulation of two back-to-back wind turbines in atmospheric boundary layer flow, *Comput. Fluids* **158** (2017) 167–175.
69. K. Takizawa, T. E. Tezduyar, S. McIntyre, N. Kostov, R. Kolesar and C. Habluetzel, Space–time VMS computation of wind-turbine rotor and tower aerodynamics, *Comput. Mech.* **53** (2014) 1–15.
70. J. Yan, X. Deng, A. Korobenko and Y. Bazilevs, Free-surface flow modeling and simulation of horizontal-axis tidal-stream turbines, *Comput. Fluids* **158** (2017) 157–166.
71. K. Takizawa, T. E. Tezduyar and N. Kostov, Sequentially-coupled space–time FSI analysis of bio-inspired flapping-wing aerodynamics of an MAV, *Comput. Mech.* **54** (2014) 213–233.
72. B. Augier, J. Yan, A. Korobenko, J. Czarnowski, G. Ketterman and Y. Bazilevs, Experimental and numerical FSI study of compliant hydrofoils, *Comput. Mech.* **55** (2015) 1079–1090.
73. J. Yan, B. Augier, A. Korobenko, J. Czarnowski, G. Ketterman and Y. Bazilevs, FSI modeling of a propulsion system based on compliant hydrofoils in a tandem configuration, *Comput. Fluids* **141** (2016) 201–211.
74. H. Suito, K. Takizawa, V. Q. H. Huynh, D. Sze and T. Ueda, FSI analysis of the blood flow and geometrical characteristics in the thoracic aorta, *Comput. Mech.* **54** (2014) 1035–1045.
75. H. Suito, K. Takizawa, V. Q. H. Huynh, D. Sze, T. Ueda and T. E. Tezduyar, A geometrical-characteristics study in patient-specific FSI analysis of blood flow in the thoracic aorta, in *Advances in Computational Fluid–Structure Interaction and Flow Simulation*: *New Methods and Challenging Computations*, eds. Y. Bazilevs and K. Takizawa, Modeling and Simulation in Science, Engineering and Technology (Springer, 2016), pp. 379–386.
76. K. Takizawa, T. E. Tezduyar, H. Uchikawa, T. Terahara, T. Sasaki, K. Shiozaki, A. Yoshida, K. Komiya and G. Inoue, Aorta flow analysis and heart valve flow and structure analysis, in *Frontiers in Computational Fluid–Structure Interaction and Flow Simulation*: *Research from Lead Investigators Under Forty – 2018*, ed. T. E. Tezduyar, Modeling and Simulation in Science, Engineering and Technology (Springer, 2018), pp. 29–89.
77. K. Takizawa, T. E. Tezduyar, H. Uchikawa, T. Terahara, T. Sasaki and A. Yoshida, Mesh refinement influence and cardiac-cycle flow periodicity in aorta flow analysis with isogeometric discretization, *Comput. Fluids* published online (2018), doi:10.1016/j.compfluid.2018.05.025.
78. T. A. Helgedagsrud, Y. Bazilevs, K. M. Mathisen and O. A. Øiseth, Computational and experimental investigation of free vibration and flutter of bridge decks, *Comput. Mech.* **63**(1) (2018) 121–136.

79. Y. Osawa, V. Kalro and T. Tezduyar, Multi-domain parallel computation of wake flows, *Comput. Methods Appl. Mech. Eng.* **174** (1999) 371–391.
80. T. Tezduyar and Y. Osawa, The multi-domain method for computation of the aerodynamics of a parachute crossing the far wake of an aircraft, *Comput. Methods Appl. Mech. Eng.* **191** (2001) 705–716.
81. T. Tezduyar and Y. Osawa, Fluid–structure interactions of a parachute crossing the far wake of an aircraft, *Comput. Methods Appl. Mech. Eng.* **191** (2001) 717–726.
82. Y. Bazilevs, J. Yan, M. de Stadler and S. Sarkar, Computation of the flow over a sphere at Re = 3700: A comparison of uniform and turbulent inflow conditions, *J. Appl. Mech.* **81** (2014) 121003.
83. S. B. Pope, Wall flows, in *Turbulent Flows* (Cambridge Univ. Press, 2000), pp. 264–332.
84. T. J. R. Hughes, J. A. Cottrell and Y. Bazilevs, Isogeometric analysis: CAD, finite elements, NURBS, exact geometry and mesh refinement, *Comput. Methods Appl. Mech. Eng.* **194** (2005) 4135–4195.
85. J. A. Cottrell, T. J. R. Hughes and Y. Bazilevs, *Isogeometric Analysis. Toward Integration of CAD and FEA* (Wiley, 2009).
86. R. Mills, J. Sheridan and K. Hourigan, Response of base suction and vortex shedding from rectangular prisms to transverse forcing, *J. Fluid Mech.* **461** (2002) 25–49.
87. A. Hatanaka and H. Tanaka, New estimation method of aerodynamic admittance function, *J. Wind Eng. Indust. Aerodyn.* **90** (2002) 2073–2086.
88. L. Patruno, Accuracy of numerically evaluated flutter derivatives of bridge deck sections using RANS: Effects on the flutter onset velocity, *Eng. Struct.* **89** (2015) 49–65.
89. T. A. Helgedagsrud, I. Akkerman, Y. Bazilevs, K. M. Mathisen and O. A. Øiseth, Isogeometric modeling and experimental investigation of moving-domain bridge aerodynamics, *J. Eng. Mech.* **145**(5) (2019) 04019026.
90. Y. Bazilevs and T. J. R. Hughes, Weak imposition of Dirichlet boundary conditions in fluid mechanics, *Comput. Fluids* **36** (2007) 12–26.
91. Y. Bazilevs, C. Michler, V. M. Calo and T. J. R. Hughes, Isogeometric variational multiscale modeling of wall-bounded turbulent flows with weakly enforced boundary conditions on unstretched meshes, *Comput. Methods Appl. Mech. Eng.* **199** (2010) 780–790.
92. M.-C. Hsu, I. Akkerman and Y. Bazilevs, Wind turbine aerodynamics using ALE-VMS: Validation and role of weakly enforced boundary conditions, *Comput. Mech.* **50** (2012) 499–511.
93. R. H. Scanlan, The action of flexible bridges under wind, I: Flutter theory, *J. Sound Vib.* **60** (1978) 187–199.
94. R. H. Scanlan, Problematics in formulation of wind force models for bridge decks, *J. Eng. Mech.* **119** (1993) 1353–1375.
95. Y. Tamura and A. Kareem (eds.) *Advanced Structural Wind Engineering* (Springer, 2013).
96. S. B. Pope, The scales of turbulent motion, in *Turbulent Flows* (Cambridge Univ. Press, 2000), pp. 182–263.
97. O. Øiseth, A. Rönnquist and R. Sigbjörnsson, Simplified prediction of wind-induced response and stability limit of slender long-span suspension bridges, based on modified quasi-steady theory: A case study, *J. Wind Eng. Indust. Aerodyn.* **98** (2010) 730–741.
98. L. Zhao and Y. Ge, Cross-spectral recognition method of bridge deck aerodynamic admittance function, *Earthquake Eng. Eng. Vib.* **14** (2015) 595–609.

99. L. Zhu, Q. Zhou, Q. Ding and Z. Xu, Identification and application of six-component aerodynamic admittance functions of a closed-box bridge deck, *J. Wind Eng. Indust. Aerodyn.* **172** (2018) 268–279.
100. Norwegian Public Roads Administration, *Handbook N400 Bridge Design* (The Norwegian Directorate of Public Roads, 2015).
101. Y. Bazilevs, K. Takizawa and T. E. Tezduyar, *Computational Fluid–Structure Interaction: Methods and Applications* (Wiley, 2013).
102. M.-C. Hsu, Y. Bazilevs, V. M. Calo, T. E. Tezduyar and T. J. R. Hughes, Improving stability of stabilized and multiscale formulations in flow simulations at small time steps, *Comput. Methods Appl. Mech. Eng.* **199** (2010) 828–840.
103. K. Takizawa, T. E. Tezduyar and Y. Otoguro, Stabilization and discontinuity-capturing parameters for space–time flow computations with finite element and isogeometric discretizations, *Comput. Mech.* **62** (2018) 1169–1186.
104. T. E. Tezduyar, Computation of moving boundaries and interfaces and stabilization parameters, *Int. J. Numer. Methods Fluids* **43** (2003) 555–575.
105. T. E. Tezduyar and Y. Osawa, Finite element stabilization parameters computed from element matrices and vectors, *Comput. Methods Appl. Mech. Eng.* **190** (2000) 411–430.
106. Y. Bazilevs, V. M. Calo, T. J. R. Hughes and Y. Zhang, Isogeometric fluid-structure interaction: Theory, algorithms and computations, *Comput. Mech.* **43** (2008) 3–37.
107. Y. Bazilevs, C. Michler, V. M. Calo and T. J. R. Hughes, Weak Dirichlet boundary conditions for wall-bounded turbulent flows, *Comput. Methods Appl. Mech. Eng.* **196** (2007) 4853–4862.
108. Y. Bazilevs and T. J. R. Hughes, Weak imposition of Dirichlet boundary conditions in fluid mechanics, *Comput. Fluids* **36** (2007) 12–26.
109. J. Chung and G. M. Hulbert, A time integration algorithm for structural dynamics with improved numerical dissipation: The generalized-α method, *J. Appl. Mech.* **60** (1993) 371–375.
110. K. E. Jansen, C. H. Whiting and G. M. Hulbert, A generalized-α method for integrating the filtered Navier–Stokes equations with a stabilized finite element method, *Comput. Methods Appl. Mech. Eng.* **190** (2000) 305–319.
111. D. B. Spalding, A signal formula for the law of the wall, *J. Appl. Mech.* **28** (1961) 444–458.
112. R. B. Dean, Reynolds number dependence of skin friction and other bulk flow variables in two-dimensional rectangular duct flow, *J. Fluids Eng.* **100** (1978) 215.
113. R. D. Moser, J. Kim and N. N. Mansour, Direct numerical simulation of turbulent channel flow up to Re = 590, *Phys. Fluids* **11** (1994) 943–945.
114. S. Hoyas and J. Jiménez, Scaling of the velocity fluctuations in turbulent channels up to Re = 2003, *Phys. Fluids* **18** (2006) 011702.
115. J. C. Kaimal, J. C. Wyngaard, Y. Izumi and O. R. Coté, Spectral characteristics of surface-layer turbulence, *Quart. J. Royal Meteorol. Soc.* **98** (1972) 563–589.
116. E. E. Morfiadakis, G. L. Glinou and M. J. Koulouvari, The suitability of the von Karman spectrum for the structure of turbulence in a complex terrain wind farm, *J. Wind Eng. Indust. Aerodyn.* **62** (1996) 237–257.
117. G. Karypis and V. Kumar, A fast and high quality multilevel scheme for partitioning irregular graphs, *SIAM J. Sci. Comput.* **20** (1998) 359–392.
118. X. Chen and A. Kareem, Advances in modeling of aerodynamic forces on bridge decks, *J. Eng. Mech.* **128** (2002) 1193–1205.
119. F. Brusiani, S. De Miranda, L. Patruno, F. Ubertini and P. Vaona, On the evaluation of bridge deck flutter derivatives using RANS turbulence models, *J. Wind Eng.* **119** (2013) 39–47.